

Banded microstructures in rapidly solidified Al-3 wt% Er

Original

Banded microstructures in rapidly solidified Al-3 wt% Er / Gianoglio, D.; Marola, S.; Battezzati, L.; Aversa, A.; Bosio, F.; Lombardi, M.; Manfredi, D.; Lorusso, M.. - In: INTERMETALLICS. - ISSN 0966-9795. - ELETTRONICO. - 119:(2020), pp. 106724-106728. [10.1016/j.intermet.2020.106724]

Availability:

This version is available at: 11583/2795874 since: 2020-02-21T02:11:01Z

Publisher:

Elsevier Ltd

Published

DOI:10.1016/j.intermet.2020.106724

Terms of use:

This article is made available under terms and conditions as specified in the corresponding bibliographic description in the repository

Publisher copyright

(Article begins on next page)

Banded microstructures in rapidly solidified Al-3 wt% Er

Dario Gianoglio, Silvia Marola, Livio Battezzati*, Dipartimento di Chimica, Università di Torino, Via Pietro Giuria 7, 10125, Torino, Italy

Alberta Aversa, Federico Bosio, Mariangela Lombardi, Diego Manfredi, Department of Applied Science and Technology, Politecnico di Torino, Corso Duca degli Abruzzi, 24, 10129, Turin, Italy

Massimo Lorusso, Istituto Italiano di Tecnologia, Center for Sustainable Future Technologies, Via Livorno, 60, 10144, Torino, Italy

*Corresponding Author: livio.battezzati@unito.it

Abstract

Banded and discontinuous eutectic microstructures were found in melt quenched ribbons and laser melted single tracks of an Al-3%wt Er alloy, respectively. The bands occurring in ribbons are made of alternate primary α -Al phase and eutectic. Their formation is well described by the Han-Trivedi model for banding in alloy solidification. Microstructure fluctuations between fibrous and discontinuous eutectic are seen in laser melted single tracks on the same length scale of bands due to change in local temperature gradient. Overall, various transitions in phase morphology are found in thin zones of material constituting a valuable guideline for interpretation of the solidification mechanism. Nano-indentation tests show that the fine microstructures induce substantial hardening.

Keywords: B. nucleation and growth, C. rapid solidification, C. laser processing, D. microstructure, F. electron microscopy, scanning, F. nanoindentation.

1. Introduction

Some rare earth elements are considered as strengtheners of Al, especially at high temperature [1]. Their chemical affinity to Al favours miscibility in the liquid state and formation of tri-aluminides in the solid state. The hardening of the Al matrix occurs in the presence of a dispersion of fine tri-aluminide particles which are thermally stable up to the liquidus [1]. Among rare-earth elements, the interest in the Al-Er system stems from the cubic structure of Al_3Er precipitates which may display a coherency relationship with the matrix. Actually, the Er appears also to promote the formation of precipitates in Al alloys containing either Sc or Li [2, 3]. Both Al_3Er [4] and cubic tri-aluminide particles of mixed Er and Zr were shown be potent retardant of recrystallization [5]. Since the tri-aluminides limit the terminal solubility of rare earths in fcc-Al, the dispersion is more frequently obtained in solidification. However, a significant hardness enhancement has been found after precipitation hardening of an alloy of composition close to the maximum Er solubility in the solid state [6]. The solubility of Er in fcc-Al was disregarded in calculations of the binary Al-Er phase diagram [7, 8]. However, both recent experimental works and first principle calculations have provided clear evidence of the trend of the solvus curve of Er in Al up to the eutectic temperature [9, 10].

In early reports rapid solidification was employed to extend the Er solid solubility in Al-10.8 wt% Er, i. e. a slightly hypoeutectic alloy [11], and Al- 4 wt% Er [12]. For both alloys an increment in hardness was demonstrated, at least up to the T4 condition [12]. The advent of additive manufacturing processes to build objects by means of selective laser melting (SLM) or electron

beam melting (EBM) [13], i. e. rapid solidification techniques, is renewing the interest in these materials. In this context, we explore here the role of minute quantity of Er in planar flow casting and single track laser melting of alloy powders following up findings on other Al alloys [14, 15]. Novel fine microstructures are found providing insight into the varied solidification mechanism of these alloys and appear of interest for dispersion hardening of the matrix in additive manufacturing processes.

2. Experimental

Al-3wt%Er (i. e. Al-0.05at% Er) atomized powder was purchased from Nanoval GmbH (Germany). Portions of powder were compacted and induction melted in a Buehler planar flow casting apparatus to produce continuous ribbons, 10 mm wide and 30-40 μm thick [15]. A single layer of powders, 50 μm thick, was spread onto a disk of commercially pure Al and melted twice by scanning a laser beam with power of 195 W, spot size of 90 μm and scanning speed of 600 mm/s in an EOSINT M270 Dual Mode equipment. Laser melted single tracks were obtained with cross section of 120 μm in width and 180 μm in height [14, 16]. The rapidly solidified samples were analysed by X-ray diffraction confirming the occurrence of the expected phases: α -Al and Al_3Er . Their microstructure was examined in cross section by means of a Field Emission Scanning Electron Microscope (FESEM, Zeiss Supra 40).

The hardness at the small scale was determined with a TI950 Nanoindenter of Hysitron. The Oliver-Pharr method was adopted to obtain the hardness from force versus displacement curves [17]. The tests on the specimens were performed by applying and removing a controlled load. A diamond Berkovich tip indenter was used, i. e. a 3-sided diamond pyramid with an included angle of 142.3° and an angle from the normal to face of 65.35° . A grid of indentations at 4 μm distance from each other was made on the cross section of specimens: a matrix of $11 \times 13 = 143$ indentations was made on ribbons, and a matrix of $22 \times 28 = 616$ indentations was made on laser melted single tracks. In each indentation, the load was increased at 150 $\mu\text{N/s}$ up to a maximum load of 2.5 mN and then decreased at the same rate. The indents were observed in FESEM in order to select only those which were completely inside the samples cross section, and to exclude those eventually influenced by the external border.

3. Results and Discussion

3.1 Er solubility in Al and phase diagram

We re-consider preliminarily the Al-rich portion of the phase diagram reported in the available assessments [7, 8] where no terminal solid solubility was assumed. Actually, a recent work has provided quantitative data on the solubility of Er in Al [10] (Fig. 1) and Er is likely to be supersaturated in Al during non-equilibrium processing. The solubility of Al_3Er in Al is represented by means of the Arrhenius equation with activation enthalpy, $Q = -0.21 \text{ eV/atom}$ (corresponding to $-82.98 \text{ kJ/mole of atoms}$ or $-20.75 \text{ kJ/mole of compound}$) and activation entropy, $3k$ with k the Boltzmann constant [10]. Assuming regular solution behaviour in the primary solid solution, the activation enthalpy equals the difference between the enthalpy of formation of the Al_3Er compound, ΔH_{form} , and the enthalpy of mixing of elements in the solid solution at infinite Al_3Er dilution, Ω , i. e. the interaction parameter of the regular solution, $Q = \Delta H_{\text{form}} - \Omega$ [18]. The thermodynamic assessment reported in [8] gives $\Delta H_{\text{form}} = -38.3 \text{ kJ/mole}$. Therefore, $\Omega = -17.5 \text{ kJ/mole}$. The free energy of the Al-rich solid solution was evaluated using this parameter. Taking the Al_3Er and liquid free energies from [8], the eutectic position and the T_0 curve were derived as shown in Fig. 1.

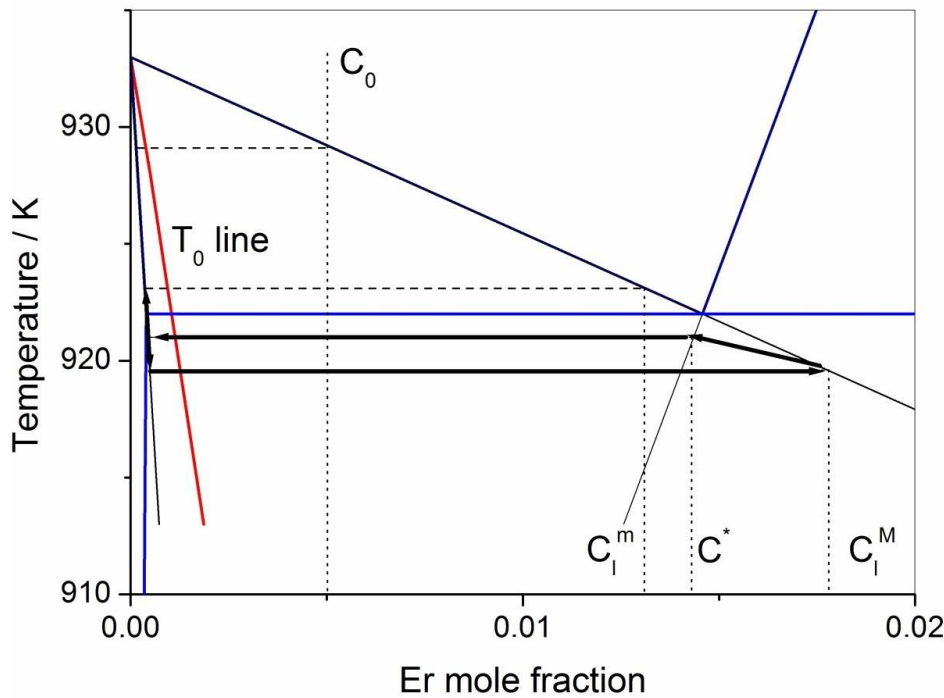


Fig. 1. The Al-rich portion of the Al-Er phase diagram reconstructed as detailed in the text. The solvus, solidus, liquidus and eutectic lines are in blue bold lines. The solidus and liquidus lines are extended in the undercooling regime. The superimposed black bold arrows show the banding cycle. Symbols are defined in the text.

The Al-Al₃Er eutectic is located at 922 K and 0.0146 mole fraction Er. The solubility at the eutectic temperature results 0.00040 mole fraction Er. In the limit of the present approximation it appears that partitionless solidification below T₀ would be possible at an undercooling of the order of 20 K which might occur at the start of solidification before the temperature increases because of heat release by recalescence. The solidification range of the alloy is anyhow limited.

3.2 Microstructures in melt spun ribbons and banding cycle.

Fig. 2 shows an etched cross section of a ribbon. Apparently, at first primary columns solidified on the wheel side on undercooling with substantial solute trapping, possibly close to the T₀ line. Solute segregation promoted the formation of the eutectic at column boundaries. The release of latent heat caused recalescence and reduction in thermal gradient inducing the transition to approximately equiaxed cells which contain internal bands developed along the direction of heat flow. The bands consist of alternated primary α -Al and Al + Al₃Er eutectic. A further columnar/eutectic microstructure, a few microns thick, then occurred along the direction of heat flow followed by dendritic/eutectic non-oriented features close to the external side of the ribbon. It is apparent that the amount of eutectic is less and the size of the columnar crystals larger close to the wheel side with respect to the opposite one, indicating solute supersaturation and larger growth rate.

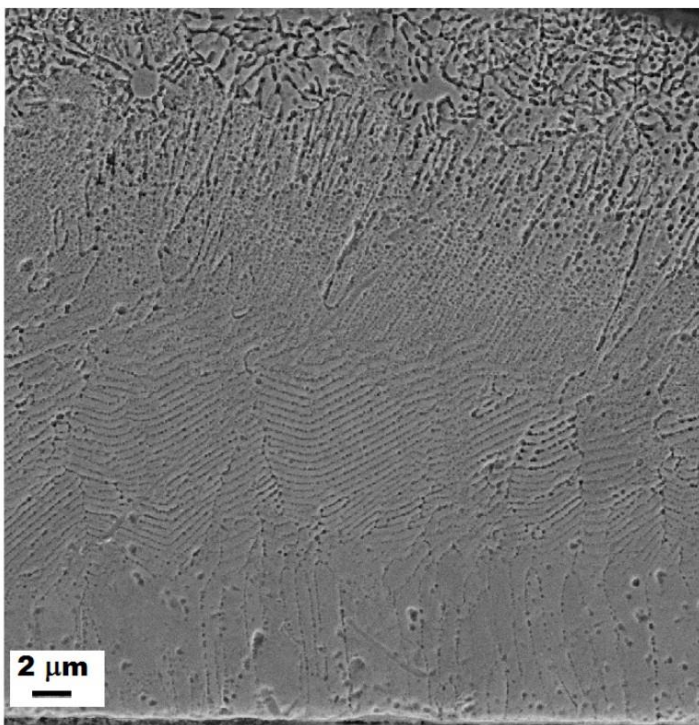


Fig. 2. The cross section of an Al-Er ribbon. The image was obtained in secondary mode after etching with Keller reagent. At the bottom of image is the wheel side, at the top the external side.

Fig. 3a shows the equiaxed banded and columnar crystals in backscattering mode: because of the difference in atomic number between Al and Er, the Al_3Er particles are clearly seen as well as contrast fluctuations in the matrix due to changes in Er concentration. The eutectic Al_3Er at grain boundaries appears fibrous and surrounded by dark zones, apparently of lower Er content. In the grain interior, the α -Al primary bands are on average solute poor. They alternate with eutectic bands which incorporate the excess solute. Actually, the fine rounded Al_3Er eutectic particles occur in correspondence of the lightest regions. Precipitates of the compound are embedded inside the α -Al band, possibly formed by self-anneal during free cooling after solidification.

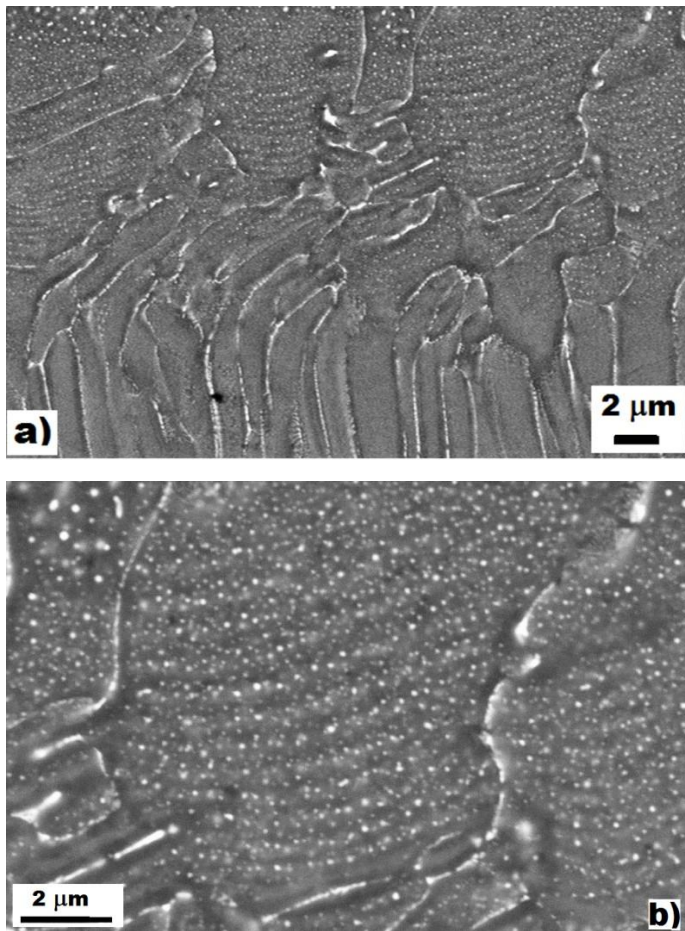


Fig. 3. a) Back-scattering electron image of the portion of the ribbon cooled at the higher rate. From bottom to top of image: wheel side, bulk of ribbon. Al-rich columns originate on the quenching wheel followed by banded equiaxed primary crystals. The white spots and elongated zones are the Al_3Er compound. Fluctuations in contrast refer to fluctuations in Er concentration. b) An enlarged view of a primary grain containing bands.

A dynamic model for the oscillations was developed by Han and Trivedi to explain the banding induced in a transparent alloy directionally solidified at various pulling velocities [19]. The model provides relationships between the width of the primary and eutectic bands, the solute concentration

in the growing solids and the respective growth velocity. The correspondence of the present microstructural results to the model is checked in the following. Since the growth rates are not experimentally determined in planar flow casting and laser quenching, an inverse procedure is used starting from the length scale of microstructural features to derive the relevant local compositions in the alloy and growth rates during banding.

The average eutectic spacing between primary and compound phases, λ , was determined from Fig. 3b to obtain an estimate of the interfacial undercooling with respect to the eutectic temperature, ΔT , according to [20]

$$\Delta T = \frac{4\gamma_{\alpha\beta}}{\lambda \Delta S} \quad (1)$$

where $\gamma_{\alpha\beta}$ is the interfacial energy between crystal phases taken as 0.22 J/m² [9] and ΔS the entropy of fusion which is taken as that of Al, 11.6 J/moleK. The average λ is 0.31 μm . The corresponding undercooling with respect to the eutectic temperature results 2.4 K. The eutectic growth rate, V , is then determined using [20]

$$V^2 = \frac{16D_L(T_I)\Delta T}{\bar{m}\Delta S\Delta C} \quad (2)$$

where $D_L(T_I)$ is the interdiffusion coefficient at the interface temperature, T_I , approximated as the self-diffusion coefficient of Al at the melting point, $5.922 \cdot 10^{-9} \text{ m}^2/\text{s}$ [21], \bar{m} is the average liquidus slope derived from the assessed phase diagram (Fig. 1) as 753.4 K/at%, and ΔC the difference in composition between the eutectic phases. The eutectic growth rate results 2.6 mm/s.

According to models for growth morphology [24], the growth rate increases during the formation of columns because of the rise in solute concentration in the liquid ahead of the interface which causes increase in constitutional supercooling and transition to cellular crystals. The growth rate approaches that of absolute stability, V_{as} , and banding sets in. Bands are oscillating structures

occurring parallel to the moving interface whose growth rate fluctuates with time because of non-equilibrium effects at the interface [23-24].¹

Taking the average width of the eutectic, λ_E , and primary bands, λ_α , measured on images such as those reported in Figs. 2 and 3, 0.26 μm and 0.32 μm , respectively, and using the same notations as in [17], the C^* concentration, i. e. the average composition in the growing eutectic solid, is derived from

$$\square_E = \frac{D_L}{V} h \frac{C_E - C_0}{C^* - C_0} \quad (3)$$

where C_E is the eutectic Er concentration, C_0 the alloy composition, D_L the diffusion coefficient in the liquid, and V the eutectic growth rate determined above. The calculation gives $C^* = 0.0143$ mole fraction Er which is expected to fall in the range of the eutectic coupled zone but close to its limit for hypoeutectic compositions [19].

The primary phase grows at a lower rate, of the order of the absolute stability limit, V_{as} . Since we are dealing with rapid solidification processes, the partition coefficient is expected to deviate from the equilibrium value. This was checked by using the result of the Aziz-Kaplan model [25] which gives the kinetic partition coefficient, k_v , as

$$k_v = \frac{k_\alpha + P_i}{1 + P_i} \quad (4)$$

where k_\square is the equilibrium partition coefficient for the α phase which is derived from the phase diagram as 0.0274, P_i is the interface Peclet number for solute redistribution defined as $P_i = a_0 V / D_i$ with a_0 an interface diffusion length taken of the order of $1 \cdot 10^{-9}$ m and D_i an interface diffusion coefficient taken of the order of the diffusion coefficient in the liquid as above. The non-equilibrium partition coefficient results higher than k_\square of about 0.7%. This is due to the low growth velocity of the primary phase at the limited undercooling deduced from the microstructure. For comparison, the velocity at the absolute **stability limit, V_{as}** [22]

¹ It is worth noting that primary phase/eutectic bands in the Al-Er system were present in the TEM picture of Fig. 2 in [11]. The bands were not discussed further. The banding phenomenon was frequently observed in Al-alloys and analyzed in detail in later works [23-24].

$$V_{as} = \frac{D\Delta S\Delta T_0}{k_\alpha\gamma_{sl}} \quad (5)$$

where ΔT_0 is the equilibrium freezing range ($\Delta T_0 = \bar{m}C_0(k_\alpha - 1)/k_\alpha$) resulting here 110.5 K, and γ_{sl} the liquid crystal interfacial energy, estimated as 0.11 Jm⁻² in a nucleation study [10] results 2.5·10⁻³ ms⁻¹. Not surprisingly, in view of the low undercooling, V_{as} is close although less than the eutectic growth rate.

As above, the width of the primary α band relates to growth rate, physical parameters, and relevant concentrations according to [19]

$$\frac{\Delta V k_\alpha}{D_L} = \ln \frac{C_l^M - C_0}{C_l^m - C_0} + \ln \frac{C_0 - k_\alpha C_l^m}{C_0 - k_\alpha C_l^M} \quad (6)$$

where C_l^M is the liquid composition at the nucleation temperature, C_l^m the liquid composition in correspondence with the minimum solute concentration in the α phase. C_l^M is read on the phase diagram (Fig. 1) at the undercooling derived from eq. 1 as 0.0178 mole fraction Er, therefore C_l^m results 0.0131 mole fraction Er.

The concentration values are reported at the respective temperatures in Fig. 1 which shows the composition path in the banding cycle. After the initial formation of the primary phase, solute rejection ahead of the moving interface shifts the liquid composition towards the zone for nucleation and coupled growth of the eutectic. Eutectic growth consumes the excess solute at the appropriate temperature. Then, the primary phase outgrows the eutectic with no re-nucleation and the oscillating process is established until the varying temperature gradient imposed by the cooling conditions allows for it. The detection of the bands in thin ribbons owes much to the small change in growth rate of phases obtained in planar flow casting. It is interesting that in the narrow space of the ribbon cross section, transitions in phase morphology are found as reported in laser surface melting experiments on Al-rich Al-Cu and Al-Fe alloys [23, 24, 26].

3.3 Microstructures in laser single tracks.

Exemplary microstructures of laser single tracks samples of Al-0.005 mole fraction Er on top of an Al substrate are shown in Fig. 4. With the experimental conditions chosen for this work the substrate melts to a limited extent, enough to anchor the molten pool (Fig. 4a). When solidification

starts, columnar crystals of the primary phase, on average 250 nm in size, grow on the pre-existing α -Al grains, very likely epitaxially, with eutectic in between because of lateral rejection of solute. Coupled growth of eutectic Al_3Er occurs in fibrous shape. Changes in size and growth direction are seen in some places; they can be justified by considering fluctuations in temperature and local composition (Fig. 4b). Intermittently, the size of primary columns decreases on average to 150 nm (Fig. 4c) and the eutectic in between becomes uncoupled [28]. This implies transition from fibrous Al_3Er crystals to slightly elongated or roundish ones which must periodically re-nucleate along the direction of heat subtraction. The spacing among these particles is of the same order as that found in the eutectic bands shown in Fig. 3. The “banded” microstructures of Fig. 4 occur orthogonally to the direction of heat flow because of the different growth mechanism with respect to the conventional bands occurring in the same direction of heat flow (Figs. 2 and 3). However, the similarity in the size of microstructural features in ribbons and single tracks suggests that growth rates are comparable.

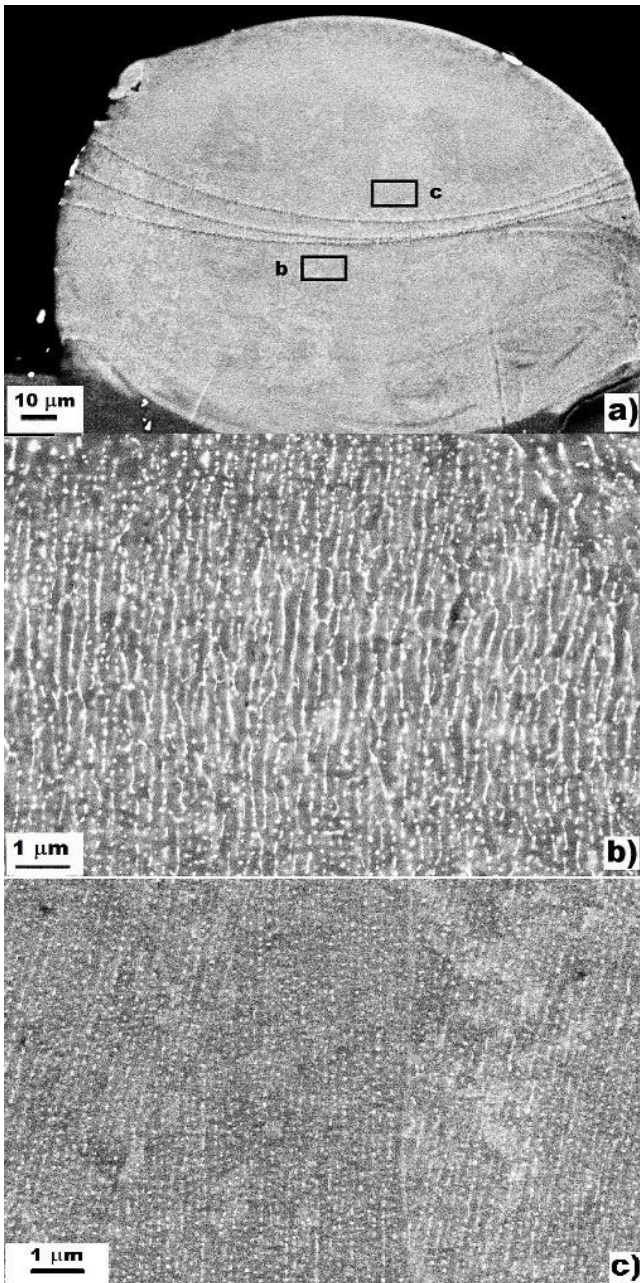


Fig. 4. Back scattering electron images of the cross section a laser scan track of Al-Er powders. a) General view of the track. The central curved features mark the repeated laser passes on the track. The heat flow direction was from top to bottom. The alloy appears homogeneous below and above them. b) and c) Enlarged views of the zones indicated on the track showing details of the fibrous (b) and uncoupled (c) eutectic grown in between primary columns. These zones extend widely in the entire re-solidified track. In c) the Al_3Er elongated or roundish particles extend in almost parallel lines in the interior of three $\alpha\text{-Al}$ grains.

It is finally noted that slight banding, 2-3 μm in thickness, was recently observed in laser melted tracks of an Al-8Ce plate intended to mimic direct energy deposition processes at a velocity of about 10 mm/s. In this case the bands contain aligned cellular/dendritic primary phase fully surrounded by a cellular/eutectic microstructure [29]. They seem akin to the regular/anomalous

eutectic bands recently reported in a CoSi-CoSi₂ alloy which developed at undercoolings between 1.6 K and 5.7 K with growth rates in the range from 0.3 to 3.8 mm/s [30].

3.4 Nano-indentation tests

A mean hardness value of 1.4 ± 0.2 GPa for the ribbons, and a mean value of 1.3 ± 0.1 GPa for the laser melted single tracks was obtained with nano-indentation tests. Examples of indents are shown in Fig. 5 in the zone of the track reported in Fig. 4c. The indents extend across several layers of eutectic phases giving a local average value for hardness.

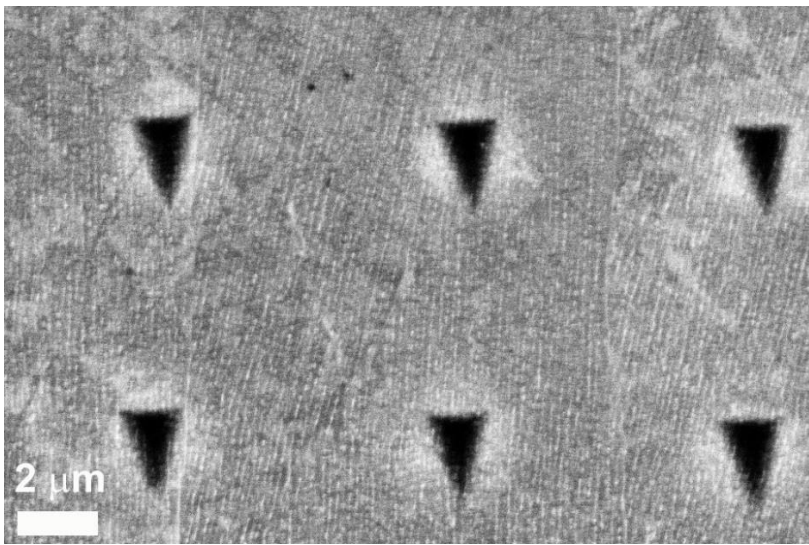


Fig. 5. Back scattering electron images of the cross section of a laser single track of Al-0.005 mole fraction Er. Indents were made in the zone reported in Fig. 4c.

As a comparison, the mean nano-hardness evaluated in previous studies on samples of AlSi10Mg alloy processed by SLM was 2.0 ± 0.15 GPa, with a corresponding Vickers micro-hardness of 135 HV0.1 and a Brinell hardness of 128 HB [31]. Using these data as reference, it is estimated that the Vickers mean values for Al-0.005 mole fraction Er should correspond to 95 ± 13 HVN for ribbons and 88 ± 7 HVN for laser melted single tracks. Compared also to literature values of precipitation hardened Al-0.00045 mole fraction Er (approximately 42 HVN) [6], the hardness achieved appears appreciable and very promising for future AM applications.

4. Conclusions

In summary, novel fine microstructures in rapidly solidified Al-Er, both melt spun ribbons and single laser scan tracks, are reported in this work and shown to comply with established solidification models for banding. Since the microstructures of additively manufactured products

are reproduced by melt spinning and single laser tracks [14, 15], the present results suggest the Al-Er system could be a candidate for building objects by means of SLM. Advantages appear provided by the limited melting range which reduces the chance of hot tearing [32] and by the solidification microstructure containing dispersion of fine intermetallic particles in the α -Al matrix giving high hardness values.

Acknowledgments

This work was supported by the regional project STAMP (Sviluppo Tecnologico dell'Additive Manufacturing in Piemonte).

References

- [1] K. E. Knipling, D. C. Dunand, D. N. Seidman, Criteria for developing castable, creep-resistant aluminum-based alloys - A review, *Zeit. fuer Metallk.*, 97 (2006) 246-265
- [2] W. Nasim, S. Yazdi, R. Santamarta, J. Malik, D. Erdeniz, B. Mansoor, D. N. Seidman, D. C. Dunand, and I. Karaman, Structure and growth of core-shell nanoprecipitates in Al-Er-Sc-Zr-V-Si high-temperature alloys, *J. Mater. Sci.*, 54 (2019) 1857-1871
- [3] T. F. Yu, B. C. Li, A. Medjahed, L. Hou, R. Z. Wua, J. H. Zhang, J. F. Sun, M. L. Zhang, Impeding effect of the $\text{Al}_3(\text{Er,Zr,Li})$ particles on planar slip and intergranular fracture mechanism of Al-3Li-1Cu-0.1Zr-X alloys, *Materials Characterization*, 147 (2019) 146-154
- [4] N. Su, R. G. Guan, X. Wang, Y. X. Wang, W. S. Jiang, H. N. Liu, Grain refinement in an Al-Er alloy during accumulative continuous extrusion forming, *Journal of Alloys and Compounds*, 680 (2016) 283-290
- [5] H. Y. Li, Z. H. Gao, H. Yin, H. F. Jiang, X. J. Su, and J. Bin, Effects of Er and Zr additions on precipitation and recrystallization of pure aluminum, *Scripta Materialia*, 68 (2013) 59-62
- [6] Y. Zhang, K. Y. Gao, S. P. Wen, H. Huang, Z. R. Nie, D. J. Zhou, The study on the coarsening process and precipitation strengthening of Al_3Er precipitate in Al-Er binary alloy, *Journal of Alloys and Compounds*, 610 (2014) 27-34
- [7] G. Cacciamani, A. Saccone, S. De Negri, and R. Ferro, The Al-Er-Mg Ternary System Part II: Thermodynamic Modeling, *Journal of Phase Equilibria*, 23 (2002) 38-50
- [8] L. L. Jin, Y.-B. Kang, P. Chartrand, C. D. Fuerst, Thermodynamic evaluation and optimization of Al-Gd, Al-Tb, Al-Dy, Al-Ho and Al-Er systems using a Modified Quasichemical Model for the liquid, *CALPHAD: Computer Coupling of Phase Diagrams and Thermochemistry*, 34 (2010) 456-466
- [9] Z. G. Mao, D. N. Seidman, C. Wolverton, First-principles phase stability, magnetic properties and solubility in aluminum-rare-earth (Al-RE) alloys and compounds. *Acta Mater.*, 59 (2011) 3659-3666
- [10] Y. Zhang, K. Y. Gao, S. P. Wen, H. Huang, W. Wang, Z. W. Zhu, Z. R. Nie, D. J. Zhou, Determination of Er and Yb solvuses and trialuminide nucleation in Al-Er and Al-Yb alloys, *Journal of Alloys and Compounds* 590 (2014) 526-534
- [11] D. Eliezer, S. J. Savage, Y. R. Mahajan, F. H. Froes, Microstructure and thermal properties of rapidly solidified Aluminum-Rare Earth alloys, in *Rapidly Solidifies Alloys and their Mechanical and Magnetic Properties*, B. C. Giessen, D. E. Polk, A. I. Taub eds., MRS Proc., vol. 58, Pittsburgh, 1986, 293-298
- [12] A. Ruder, D. Eliezer, Microstructure and thermal stability of a rapidly solidified Al-4Er alloy, *J. Mat. Sci.*, 25 (1990) 3541-3545
- [13] M. Tang, P. C. Pistorius, S. Narra, J. L. Beuth, Rapid Solidification: Selective Laser Melting of AlSi10Mg, *JOM*, 68 (2016) 960-966.

- [14] F. Bosio, A. Aversa, M. Lorusso, S. Marola, D. Gianoglio, L. Battezzati, P. Fino, D. Manfredi, M. Lombardi, A time-saving and cost-effective method to process alloys by Laser Powder Bed Fusion, *Materials and Design*, 181 (2019) 107949
- [15] S. Marola, D. Manfredi, G. Fiore, M. G. Poletti, M. Lombardi, P. Fino, L. Battezzati, A comparison of Selective Laser Melting with bulk rapid solidification of AlSi10Mg alloy *Journal of Alloys and Compounds*, 742 (2018) 271-279.
- [16] N. T. Aboulkhair, I. Maskery, C. Tuck, I. Ashcroft, N. M. Everitt, On the formation of AlSi10Mg single tracks and layers in selective laser melting: Microstructure and nano-mechanical properties, *Journal of Materials Processing Technology*, 230 (2016) 88–98.
- [17] W.C. Oliver, G.M. Pharr, Journal of Materials Research, An improved technique for determining hardness and elastic modulus using load and displacement sensing indentation experiments, *Journal of Materials Research*, 7 (1992) 1564-1583.
- [18] D.A. Porter, K. E. Easterling, M. Y. A. Sherif, *Phase Transformations in Metals and Alloys*, CRC Press, Boca Raton, FL, USA, 2009.
- [19] S.H. Han, R. Trivedi, Banded Microstructure Formation in Off-Eutectic Alloys, *Met. Mat. Trans. A*, 31A (2000) 1820-1832
- [20] W. J. Boettinger, *Growth kinetic limitations during rapid Solidification*, in *Rapidly Solidified Amorphous and Crystalline Alloys*, B. H. Kear, B. C. Giessen, and M. Cohen Eds, Elsevier, 1992, p. 15 - 31.
- [21] F. Demmel, D. Szubrin, W.-C. Pilgrim, C. Morkel, Diffusion in liquid aluminium probed by quasielastic neutron scattering, *Phys. Rev. B*, 84 (2011) 014307
- [22] R. Trivedi, W. Kurz, Dendritic Growth, *Intern. Mater. Rev.*, 39 (1994) 49-74
- [23] S. C. Gill, W. Kurz, Rapidly solidified Al-Cu alloys - I. Experimental determination of the microstructure selection map, *Acta metall, mater.*, 41 (1993) 3563-3573
- [24] P. Gilgien, A. Zryd, W. Kurz, Microstructure selection map for Al-Fe alloys, *Acta metall, mater.*, 43 (1995) 3477-3487
- [25] M.J. Aziz, T. Kaplan, Continuous growth model for interface motion during alloy solidification, *Acta Metall.*, 36 (1988) 2335-2347
- [26] S. C. Gill and W. Kurz, Rapidly solidified Al-Cu alloys - 2. calculation of the microstructure selection map, *Acta Metall. Mater.*, 43 (1995) 139-151.
- [27] J. T. McKeown, A. K. Kulovits, C. Liu, K. Zwiack, B. W. Reed, T. LaGrange, J. M.K. Wiezorek, G. H. Campbell, In situ transmission electron microscopy of crystal growth-mode transitions during rapid solidification of a hypoeutectic Al-Cu alloy, *Acta Mater.*, 65 (2014) 56-68.
- [28] W. Kurz, D.J. Fischer, *Fundamentals of Solidification*, Trans Tech Pub, Aedermannsdorf, Switzerland, 1986.

[29] A. Plotkowski, O. Rios, N. Sridharan, Z. Sims, K. Unocic, R.T. Ott, R.R. Dehoff, S.S. Babu, Evaluation of an Al-Ce alloy for laser additive manufacturing, *Acta Mater.*, 126 (2017) 507-519.

[30] G. Fiore, A. Quaglia, L. Battezzati, Banded regular/anomalous eutectic in rapidly solidified Co-61.8 at.% Si, *Scripta Materialia*, 168 (2019) 100–103.

[31] A. Aversa, M. Lorusso, G. Cattano, D. Manfredi, F. Calignano, E.P. Ambrosio, S. Biamino, P. Fino, M. Lombardi, M. Pavese, A study of the microstructure and the mechanical properties of an Al-Si-Ni alloy produced via selective laser melting, *Journal of Alloys and Compounds*, 695 (2017) 1470-1478.

[32] J. H. Martin, B. D. Yahata, J. M. Hundley, J. A. Mayer, T. A. Schaedler, T. M. Pollock, 3D printing of high-strength aluminium alloys, *Nature*, 549 (2017) 365-370.